RANGE MONITORING CAPABILITIES WITH THE SiFi-CC DETECTOR: SPECTRAL-SPATIAL IMAGING WITH MONTE CARLO-SIMULATED DATA*

Jorge Roser, Magdalena Rafecas

Institute of Medical Engineering, University of Lübeck, Germany

Ronja Hetzel, Philippe Clement, Alexander Fenger
Jonas Kasper, Linn Mielke, Achim Stahl

RWTH University, Aachen, Germany

Monika Kercz, Magdalena Kołodziej, Katarzyna Rusiecka
Aleksandra Wrońska

Institute of Physics, Jagiellonian University, Kraków, Poland

Received 30 August 2024, accepted 15 October 2024,
published online 27 November 2024

The SiFi-CC group is developing a scintillating-fiber-based Compton camera for high-efficiency gamma-ray imaging, specifically tailored for online range verification in particle therapy. After thorough optimization studies, including the development of neural-network approaches for event selection, the capability of the prototype for detecting range deviations is being studied by using realistic Monte Carlo simulations. We have implemented a spectral-spatial reconstruction based on the LM-MLEM algorithm and spectral analytical models for the system matrix and the sensitivity. In this work, we show the reconstructed images obtained from the irradiation of PMMA phantoms with 4×10^9 protons at therapeutic energies. The results show the capability of the SiFi-CC detector prototype to recover the 4.44 MeV prompt-gamma line and to detect 5 mm Bragg peak shifts.

DOI:10.5506/APhysPolBSupp.17.7-A9

1. Introduction

Particle therapy is a cancer treatment technique based on patient irradiation with ion beams which is under constant expansion, with 136 facilities

* Presented at the 5th Jagiellonian Symposium on *Advances in Particle Physics and Medicine*, Cracow, Poland, June 29–July 7, 2024.

currently in clinical operation and 69 more under construction or in a planning stage [1]. In contrast to conventional radiotherapy, conducted with photon beams, the charged particles used in particle therapy stop in the tumor region depositing there most of the imparted dose, in what is known as the Bragg-peak phenomenon. By exploiting the Bragg peak, particle therapy can reduce the dose to healthy tissue without changing the prescribed tumor dose; in addition, particle therapy offers room for optimization of the conformity of the delivered dose distribution to the tumor region. In spite of these potential advantages, the conformal nature of the Bragg peak implies a higher sensitivity of the delivered dose distribution to unexpected perturbations, which are triggered as a consequence of the uncertainty associated with the CT-to-stopping-power ratio calibration (3–3.5 % of the particle range [2, 3]), and also by other factors such as anatomical changes or by the beam delivery system. Consequently, many research groups study the feasibility of an online range verification method for particle therapy, able to detect unexpected variations of the delivered dose (intra- or interfractions). Most of the proposed range verification methods are based on the detection of secondary by-products originated after the passage of the beam particles in the patient, such as thermoacoustic emissions [4], neutrons [5], electrons [6], annihilation photons suitable for PET detection [7], and Prompt Gammas (PG). The latter are gamma-rays that arise as a consequence of the beam particle nuclear inelastic interactions within the patient, and whose spatial emission distribution is correlated with the depth-dose profile. Among the different detection candidates under investigation [8], Compton cameras (CC) represent a compact solution that does not require physical collimation and which is attracting attention in several areas of medical physics [9–11]. Such a device is being developed in the SiFi-CC project together with a coded mask prototype [12], both with the purpose to serve as a tool for online range verification in particle therapy.

2. Materials and methods

2.1. The SiFi-CC prototype: simulations and data processing

The SiFi-CC setup under development consists of two modules composed by LYSO fibers of $100 \times 1 \times 1$ mm^3 each and read out by Silicon Photomultipliers (SiPMs) in both ends of the fiber elongated direction (the X-dimension in this work). The fibers are stacked in XY-layers comprising 76 fibers with 1.3 mm pitch. The first CC module (or *scatterer*) features 16 such layers and measures $100 \times 98.5 \times 20.5$ mm^3; the second CC module (or *absorber*) features 36 layers and measures $100 \times 98.5 \times 46.5$ mm^3. In the modules, each alternate XY-layer is shifted by 0.65 mm in order to reduce the effect of the fiber pitch. Further details of the CC geometry can be found in [13, 14].

The described CC was modeled in the Geant4 simulation toolkit (version 10.4.p03) together with a cylindrical PMMA phantom (radius 100 mm) located 150 mm away in the Z-dimension from the first module; the distance between the modules was set to 120 mm (both center-to-center). The PMMA was irradiated with a 130 MeV proton beam impinging in the Y-dimension. The beam was modeled following the features found in the Cyclotron Centre Bronowice cyclotron-based treatment facility, including a bunched time structure with the extraction time of 0.8 ns (100 protons per bunch) and cycle time of 9.9 ns, as well as an elliptical, Gaussian shape ($\sigma_X = 2.97$ mm, $\sigma_Z = 2.72$ mm) and Gaussian smearing of the beam energy ($\sigma_E = 0.2$ MeV). More details can be found in [14, 15]. A scheme of the described setup can be seen in figure 1 (left).

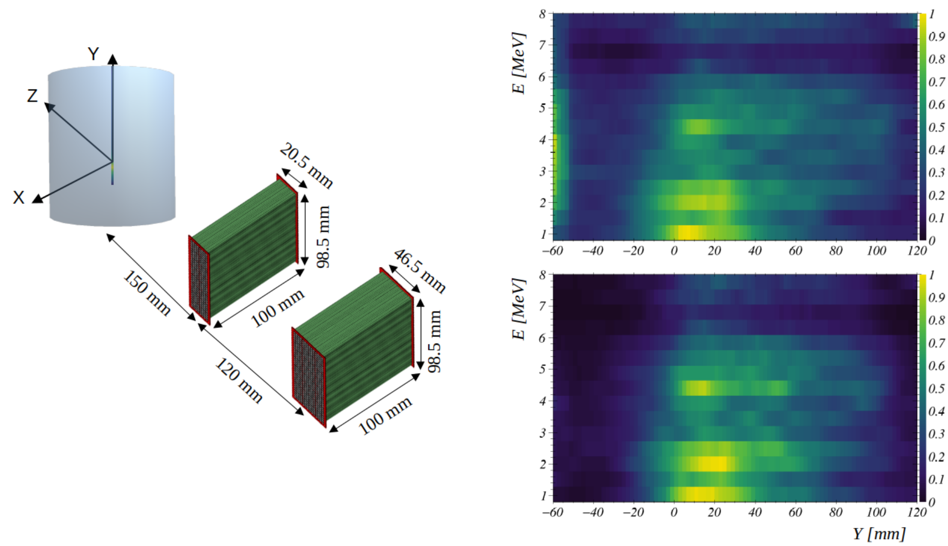

Fig. 1. Left: simulated setup. Right: YE-slice at $(X = 0 \text{ mm}, Z = 0 \text{ mm})$ after summation over the three closest X-neighbors and the closest Z-neighbor in both directions, with all the data (top) and GNN-selected data (bottom), at position A.

Two additional simulations with different phantom lengths were performed in such a way that the Bragg peak of the depth-dose distribution was shifted 5 and 10 mm from the original position. In all three positions (henceforth referred to as A, B, and C), 4×10^9 protons were used.

The simulations were carried out in a multi-stage framework that included the proton transport in the phantom, the PG production and interaction in the CC modules and the transport of optical photons in the scintillating fibers. As detailed in [14], the SiPM information resulting from the aforementioned framework is fed into a low-level reconstruction in order to obtain CC coincidence events, thus providing the input for the image reconstruction algorithm. In addition, images were also obtained upon application of an event selection strategy based on Graph Neural Networks (GNN) [16] as a previous step to image reconstruction.

2.2. Image reconstruction

Image reconstruction was performed by means of the List Mode Maximum Likelihood Expectation Maximization algorithm (LM-MLEM). Given the polychromatic nature of the PG emission and the subsequent uncertainty over the incoming gamma-ray energy, a four-dimensional image space was assumed, so that the algorithm is capable of jointly recovering the spectral-spatial PG emission distribution. To this end, the analytical models for the system matrix and the sensitivity proposed in [17] were applied. The spatial part of the image space was discretized into $41 \times 90 \times 7$ voxels with dimensions $3 \times 2 \times 3$ mm^3, whereas the spectral part was restricted to $[0.8, 8.0]$ MeV (*i.e.* the range where the most important PG lines are expected) and discretized into 15 bins. Images were obtained after 20 iterations of the algorithm and upon application of a median filter after the final iteration.

3. Results and discussion

Figure 1 (right) shows two-dimensional spectral-spatial slices extracted from the obtained images with the position A dataset. The slices show several interesting features. First, a high-intensity spot is recovered in the spectral bin containing 4.44 MeV, which is expected as this energy corresponds to an important PG line coming from the deexcitation of ^{12}C, and which is known to be well-correlated to the Bragg peak [18]. Another high-intensity region is recovered around 2 MeV. Despite the presence of PG lines at 2.00 and 2.12 MeV, this region of the four-dimensional images is contaminated by the presence of 2.22 MeV neutron capture gamma rays, not correlated to the Bragg peak. Secondly, each spectral bin features a different intensity distribution, a result which is consistent with the well-known variation in the correlation of the different PG lines with the depth-dose profile. Finally, the application of the event selection strategy results in a qualitative improvement of the obtained images, whereby edge artifacts are eliminated from the slices and more intensity is recovered in the 4.44 MeV spectral bin.

Figure 2 (left) shows, for each simulated position, the XY-slices extracted at the 4.44 MeV spectral bin; furthermore, figure 2 (right) shows the Y-profiles obtained from these slices. Again, the event selection strategy is shown to improve the quality of the images, but in all cases, a displacement of the PG spatial emission distribution can be appreciated. Quantitative

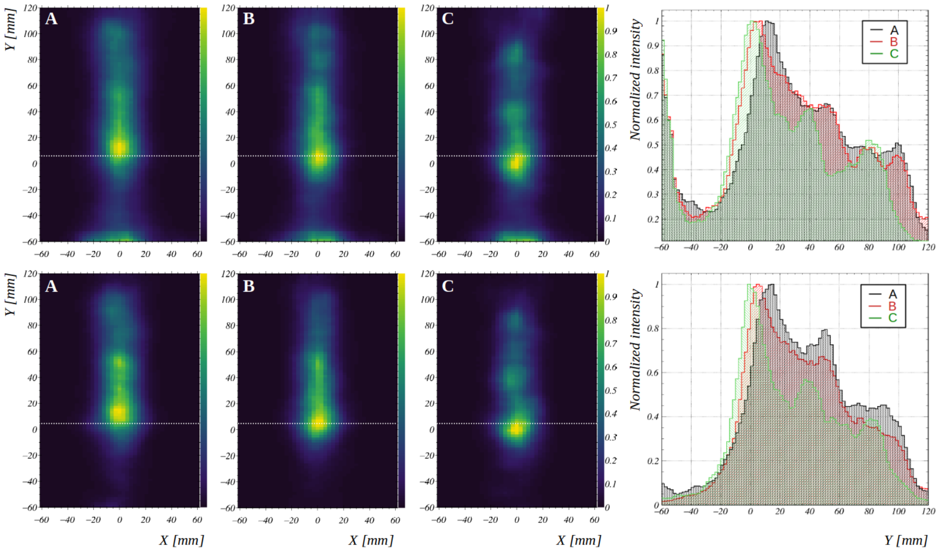

Fig. 2. Left: XY-slices at $(Z = 0 \text{ mm}, E = 4.44 \text{ MeV})$ after summation over the closest Z-neighbor in both directions. The white dashed lines indicate the maximum of position B. Right: Y-profiles at $X = 0$ mm extracted from the previously presented XY-slices, after summation over the three closest X-neighbors. Top row figures were obtained with all the data; bottom figures were obtained with GNN-selected data.

results are provided in Table 1, in which the Y-values corresponding to 80% and 50% of the intensity after the maximum (R80 and R50, respectively, *cf.* [19, 20]) are obtained by using linear interpolation. These results show that the application of the event selection strategy improves the compatibility of the obtained R80 and R50 displacements with the ground truth simulated shifts (*i.e.* 5 mm). The results allow for asserting the capability of SiFi-CC to reliably detect 5 mm depth-dose shifts with events detected after irradiation with 4×10^9 protons, higher than the clinically expected scenario. Consequently, further studies on lower statistics, including their impact on the range shift uncertainty, are needed. In addition, the capability of SiFi-CC to detect smaller range shifts (ideally below 1–2 mm [21]) remains to be tested. In spite of these requirements, the potential of the spectral-spatial imaging algorithm as a tool for range verification with CCs is endorsed, in agreement with [20].

Table 1. Y-shifts obtained from pairs of simulated positions with all the data and with GNN-selected data. Shift error values were derived from the propagation of the R80 and R50 position differences, taking only into account the voxel size as a source of uncertainty.

Positions	Data	ΔR80 $\pm$ 1.4 mm	ΔR50 $\pm$ 1.4 mm
A–B	All	6.8	6.6
A–B	GNN	5.2	4.5
B–C	All	2.8	2.1
B–C	GNN	4.1	3.9

4. Conclusions

A four-dimensional image reconstruction algorithm has been successfully applied to data obtained from detailed simulations of the detection of prompt gammas with the SiFi-CC prototype, after irradiatation of a PMMA phantom with 4×10^9 protons modeled as a beam with clinical features. The results show the capability of the algorithm to obtain spatial-spectral images consistent with the expected PG distribution and allow for recovering displacements consistent with the 5 mm simulated values; in addition, the obtained images and displacements are shown to improve after the application of an event selection strategy based on Graph Neural Networks.

This work was partly funded by the German Research Foundation (Grant COMMA, No. 383681334); by the HLRN, project No. shp00028; and by the National Science Centre (NCN), Poland (grant No. 2017/26/E/ST2/00618).

REFERENCES

[1] Particle Therapy Co-Operative Group, `https://www.ptcog.site`

[2] H. Paganetti, *Phys. Med. Biol.* **57**, R99 (2012).

[3] V.T. Taasti *et al.*, *Phys. Imaging Radiat. Oncol.* **6**, 25 (2018).

[4] K.C. Jones *et al.*, *Phys. Med. Biol.* **63**, 025018 (2018).

[5] K.S. Ytre-Hauge, K. Skjerdal, J. Mattingly, I. Meric, *Sci. Rep.* **9**, 2011 (2019).

[6] T. Yabe *et al.*, *Phys. Med.* **99**, 130 (2022).

[7] V. Ferrero *et al.*, *Sci. Rep.* **8**, 4100 (2018).

[8] A. Wrońska, D. Dauvergne, in: J. Iwanczyk, K. Iniewski (Eds.) «Radiation Detection Systems», *CRC Press/Routledge*, Boca Raton 2021, pp. 139–160.

[9] J. Roser, F. Hueso-González, A. Ros, G. Llosá, in: J. Iwanczyk, K. Iniewski (Eds.) «Radiation Detection Systems», *CRC Press/Routledge*, Boca Raton 2021, pp. 161–197.

[10] M. Uenomachi, K. Shimazoe, H. Takahashi, *Bio-Algorithms Med-Systems* **18**, 120 (2022).

[11] G. Llosá, M. Rafecas, *Eur. Phys. J. Plus* **138**, 214 (2023).

[12] R. Hetzel *et al.*, *Phys. Med. Biol.* **68**, 245028 (2023).

[13] J. Kasper *et al.*, *Phys. Med.* **76**, 317 (2020).

[14] J. Kasper *et al.*, submitted to *Phys. Med. Biol.*, 2024.

[15] A. Wrońska *et al.*, *Phys. Med.* **88**, 250 (2021).

[16] P.W. Battaglia *et al.*, `arXiv:1806.01261 [cs.LG]`.

[17] E. Muñoz *et al.*, *Phys. Med. Biol.* **65**, 025011 (2020).

[18] L. Kelleter *et al.*, *Phys. Med.* **34**, 7 (2017).

[19] P.G. Ortega *et al.*, *Phys. Med. Biol.* **60**, 1845 (2015).

[20] E. Muñoz *et al.*, *Sci. Rep.* **11**, 1 (2021).

[21] G. Pausch *et al.*, *Nucl. Instrum. Methods Phys. Res. A* **954**, 161227 (2020), Symposium on Radiation Measurements and Applications XVII.